Journal of Cleaner Production 380 (2022) 135017

Contents lists available at ScienceDirect

Journal of Cleaner Production

journal homepage: www.elsevier.com/locate/jclepro

Fracture modeling of rubber-modified binder based on Discrete Element Method

Xunhao Ding [a,*], Punyaslok Rath [b], Oliver Giraldo-Londoño [b], William G. Buttlar [b], Tao Ma [a]

[a] School of Transportation, Southeast University, 2 Sipailou, Nanjing, Jiangsu, 210096, China
[b] Department of Civil & Environmental Engineering, University of Missouri-Columbia, Columbia, MO, 65203, United States

A R T I C L E I N F O

Handling Editor: Zhen Leng

Keywords:
Discrete element method
GTR modified binder
Fracture mechanism
Cohesive zone modeling

A B S T R A C T

This study investigates the effects of rubber on anti-crack resistance for binders at the low temperature based on Discrete Element Method (DEM). Based on the commercial software Particle Flow Code (PFC), cohesive zone modeling (CZM) and viscoelastic modeling were combined for predicting the behavior of unmodified and Ground Tire Rubber (GTR) modified binders. A new binder fracture test was designed and further simulated in PFC to reveal the interactions between the rubber and binder particles. Then, fracture analysis was conducted in different aspects, including fracture energy, Load-CMOD curves which are mechanics indices, evolutions of crack length, crack number and fracture process zone (FPZ) etc., which are morphological indices. Results from simulations show that the rubber particles play an important role in improving the anti-crack performance of binders at the low temperature. The rubber modified binder will have a ductile failure mode rather than brittle one of unmodified binder, resulting in higher fracture energy. The evolutions of micro-cracks, FPZ and dissipated energy are significantly influenced by rubber particles, which explain the reason for better post-peak behavior, larger peak load of GTR modified binder in macro fracture tests.

1. Introduction

Ground Tire Rubber (GTR) has been widely used to modify asphalt mixtures for decades due to its environmental sustainability and performance benefits (Rath et al., 2019a, 2019b). GTR-modified mixtures can be manufactured using either a wet or dry process (Sienkiewicz et al., 2017). In either case, the physical reaction between the asphalt binder and rubber leads to the swelling of rubber particles, which in turn results in a significant change of physical properties in asphalt mastic and mixture systems. In this study, the wet process was applied in following process.

The modified mixtures have been shown to have an improved rutting and cracking performance compared to the conventional mixtures. In fact, modern GTR mixtures have shown similar performance to the styrene-butadiene-styrene (SBS)-modified mixtures in terms of rutting and cracking (González et al., 2010). Research has shown that the incorporation of GTR in asphalt mixtures showed a different toughening mechanism compared to the polymer-modified mixtures. To further elaborate, an SBS-modified mixture forms an internal network in the binder phase that helps increase the stiffness of the mix. On the other hand, GTR particles largely cannot be dissolved completely in the mixtures which results in toughening mechanisms that are in-line with particle inclusions in media (asphalt binder/mixture in this case) such as crack pinning.

While both laboratory and field performance of GTR mixtures is well-documented, the heterogeneous composition of GTR-modified mixtures hinders an in-depth investigation of its toughening mechanisms at a micro-scale. Using existing experimental methods, only macro-level properties of GTR-modified binders/mixtures have been evaluated in prior research (Lee et al., 2008). Wang et al. used notched semi-circular bending (SCB) test to investigate the fracture performance of crumb rubber modified (CRM) asphalt mixtures. In their studies, image processing technology was applied to obtain cracking length and its correlation with fatigue number was developed. Conclusions were made that CRM mixtures had a longer fatigue life and lower crack growth rate than unmodified ones (Wang et al., 2013). The three-point bending test was utilized in Mull's studies for evaluating fracture resistance of CRM mixtures (Mull et al., 2002). The J-integral concept was set as assessment criteria and the experimental results indicated that the J value of CRM mixtures is twice that of control ones. Thus, it is also proved that

* Corresponding author.
E-mail addresses: 101013093@seu.edu.cn (X. Ding), prath@mail.missouri.edu (P. Rath), ogiraldo@missouri.edu (O. Giraldo-Londoño), buttlarw@missouri.edu (W.G. Buttlar), matao@seu.edu.cn (T. Ma).

https://doi.org/10.1016/j.jclepro.2022.135017
Received 29 June 2022; Received in revised form 7 October 2022; Accepted 28 October 2022
Available online 2 November 2022

rubber has a positive effective in improving fracture resistance. Similar findings are also proposed by other researchers and are summarized in previous literature (Yuan et al., 2020; Yan et al., 2020). However, these macro performance indices cannot illustrate the micro-mechanism of rubberized asphalt mastic and it is really hard to reveal interactions between the rubber and binder particles from a further smaller scale based on current experimental methods.

To investigate the micro-mechanism of asphalt cracking, many researchers used high precision detection equipment, such as scanning electron microscope (SEM), X-ray scanning (CT), digital image correlation technology (DIC) and Acoustic Emission Technique (Behnia et al., 2016; Braz et al., 2011; Buttlar et al., 2014; Dave et al., 2011; Ding et al., 2019; Hill et al., 2017). These high-tech devices can well capture the crack appearances but cannot distinguish rubber particles easily at the same time and have constraints in testing conditions, limiting their use to study rubber modification successfully. As compared to experimental campaigns, numerical methods allow the mechanism investigation of heterogeneous material from a far smaller scale. Among these, the Finite-Element Method (FEM) is one of the most popular techniques based on elastic continuum theory (Gilbert Strang, 1974). Cracking analysis has been widely conducted in FEM commercial software such as Abaqus, Ansys which can well handle these fracture problems. Many researchers applied FEM in cracking study of asphalt mastic, mixture and achieve some progress from different scale. Gajewski and Sadowski analyzed crack propagation in pavement bituminous layered structures based on 2D FEM. Crack propagation sensitivity was studied and influences of bituminous layer's thickness on crack path were found based on their results (Gajewski and Sadowski, 2014). Fan proposed a new method in FEM to calculate energy release rate for crack growth (Fan et al., 2007). The simulation results show good agreement with experimental data which verified the use of Abaqus routine. Lancaster modeled SCB test by FEM and characterized the crack behavior by adding a fractional viscoelastic element in it. Inter-conversion between the creep and relaxation is accomplished by use of fractional calculus, and is validated by comparison with laboratory results (Lancaster et al., 2013). However, due to the principle of FEM, heterogeneous modeling is hard to achieve completely and rubber particles cannot be developed in FEM software directly. Thus, as an alternative method, modified binder is always developed as a whole in FEM and characterized by different groups of viscoelastic parameters. The interactions between the additions and neat binder cannot be revealed visibly (Imaninasab et al., 2016; Themeli et al., 2016).

Different from FEM, the discrete-element method (DEM) developed by Cundall has been utilized by various researchers to characterize micro-scale fracture behavior in asphalt mixtures (Cundall & Strack., 1980; Kim et al., 2008; You, 2003). As a powerful numerical modeling scheme, DEM can not only develop user defined constitutive models same as FEM (Wang & Buttlar,2019), but also simulate inter-particle behavior directly which is hard to realize in FEM (Abbas et al., 2007; Ding et al., 2020). Kim et al. and Song et al. applied cohesive zone model in DEM routine to simulate the fracture behavior of unmodified binders based on different experimental tests, including single-edge notched beam (SE (B)) test, DC (T) test and SCB test (Kim et al., 2008; Kim & Buttlar,2009; Song et al., 2015). Zhang fractured virtual specimens based on IDEAL-CT test with the help of bonding model in DEM and revealed the mechanism by comparing different gradations (Zhang et al., 2016). All of these studies show DEM has the ability to characterize fracture behavior of mixtures and can demonstrate crack appearances accurately at far more smaller scale. Although DEM can characterize the inter-particle behavior due to its discrete hypothesis, only interactions between the aggregates and asphalt in unmodified binders have been studied thus far. There are no studies for modified binders, especially modeling micro additives directly at a further smaller scale.

The objective of this study is to investigate the fracture mechanism of GTR-modified binder at the low temperature based on DEM and a new asphalt mastic fracture test. To isolate the effect of rubber particles, new fracture test was designed in laboratory and then accurate simulations were conducted based on DEM. During the simulations, rubber particles were modeled directly and their effect on the fracture behavior of binders at the low temperatures was analyzed from the perspective of micro scale.

2. Methodology and experimental

2.1. Materials

A PG64-22 binder, obtained from Illinois, was selected as a base binder and its properties were tested according to ASTM D6648 (American Society for Testing and Materials International, 2016) and ASTM D4402 (American Society for Testing and Materials International, 2000), as shown in Table 1. Dry ground rubber tire particles, 30-mesh in size were obtained, and modified binder was made by mixing the rubber particles with base asphalt under high shear speed for 30 min at 176 °C. Three GTR-modified binders with rubber content of 8%, 10% and 12% by weight of binder were prepared in the laboratory.

2.2. Experimental test

For this study, two experimental tests were conducted including the standard Bending Beam Rheometer (BBR) test at −12 °C and a new binder fracture test at −22 °C. The BBR test was used for obtaining viscoelastic parameters of binders at the low temperature and was set up as shown in Fig. 1.

The new binder fracture test was developed for cracking evaluation based on fracture mechanics principles, closely following the DC(T) test (American Society for Testing and Materials International,2013a). The DC(T) mixture test was designed following the ASTM E399 (American Society for Testing and Materials International,2013b), often used for fracture characterization of metals. A compact tension (CT) geometry was adopted for mastic testing, based on previous literature (Hakimzadeh et al., 2017). As shown in Fig. 2(a), an aluminum mold was used to cast asphalt binder specimens of dimensions 145 × 139.2 × 40 mm. Two loading holes and a notch creating insert were placed in the mold before pouring the binder. After the GTR-modified binders were poured into the mold, the specimens were kept at room temperature for 90 min, and then placed in a cooling chamber at −15 °C for 30 min before demolding, as shown in Fig. 2(b). The binder CT specimen was fractured at −22 °C and crack mouth opening displacement (CMOD) was controlled at a rate of 0.2 mm/min. The load-CMOD curves were recorded to evaluate the low-temperature cracking resistance of GTR-modified binders according to specification (American Society for Testing and Materials International, 2013a). The test is referred as the binder CT test hereafter and more details about results were obtained from Rath's study (Rath et al., 2022). This study is focused on DEM simulation of the binder CT test, as discussed in the following sections.

Table 1
Selected properties of Illinois PG64-22 binder.

Rotational Viscometer	Viscosity (Pa.s) 135 °C		Viscosity (Pa.s) 165 °C	
	0.084		0.023	
BBR at −12 °C	Stiffness (MPa) 162		m-value 0.365	
Aging levels DSR* Critical Temperature (AASHTO T315)	Unaged 66.2 °C	RTFO 72.8 °C	PAV 19.6 °C	
MSCR at 64 °C	Jnr,3.2 (kPa^{-1})	Jnr,0.1 (kPa^{-1})	Jnr, diff (%)	Recovery (%)
	2.8	2.5	12	0.195

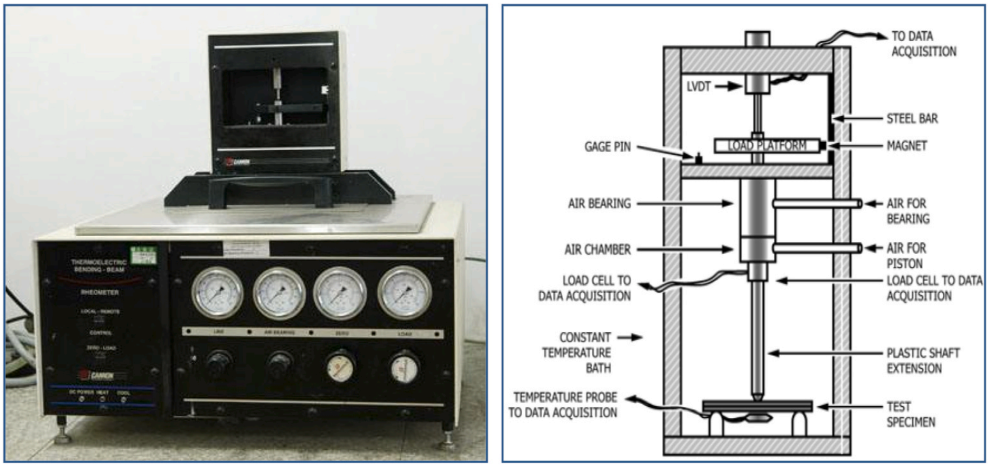

(a) (b)

Fig. 1. Bending Beam Rheometer Test:(a) apparatus; (b) schematic.

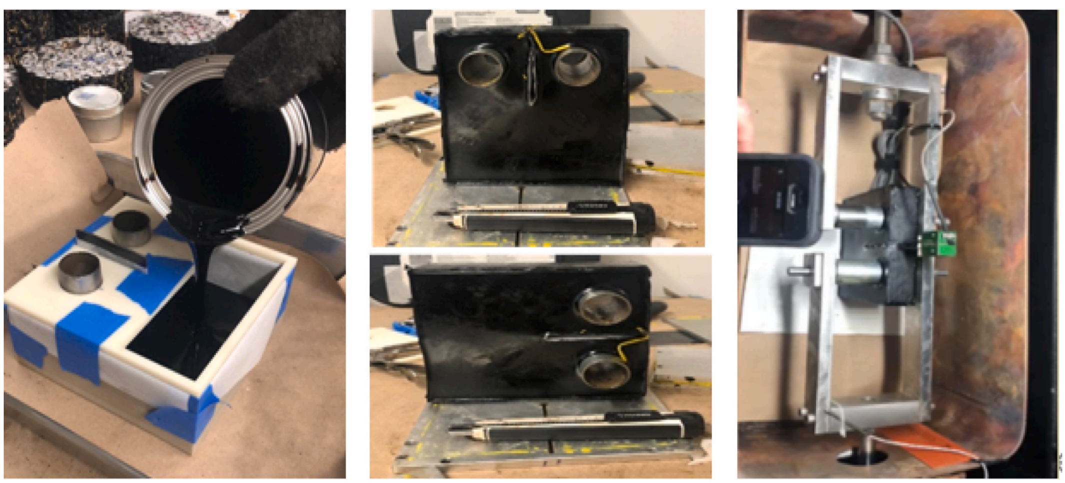

(a) (b) (c)

Fig. 2. Binder CT test design: (a) test mold; (b) binder specimens; (c) loading construction.

2.3. Constitutive models

For development of DEM simulations, several constitutive models were used based on the PFC2D manual (Itasca Consulting Group,2008), including slipping model, bonding model, Burger's model and Cohesive Zone model. The slipping model is defined by the friction coefficient μ and characterizes the friction behavior in DEM. The definition of slipping model is shown in Equation (1). The slipping model is an intrinsic property of the two balls in contact. It provide no normal strength in tension and allows slip to occur by limiting the shear force. When the shear force exceeds the maximum value, the slipping model is active automatically as Equation (1) shown.

$$F^S_{max} = \mu \left| F^n_i \right| \tag{1}$$

where, F^s_{max} is the maximum allowable shear contact force; F^n_i is the normal contact force between the two entities; μ is the friction coefficient.

Bonding models allow particles to be bonded together at contact and the presence of them inactivates the slipping model. In DEM, there are two basic forms of bonding model known as contact bond model and parallel bond model respectively. The contact bond acts only at the contact point with small size while the parallel bond acts over a cross-section. For this study, contact bond model was selected to glue particles out of the region of interest (ROI) and strength in normal/shear directions were set then for simulations.

Burger's model has been verified by some researchers as an adequate characterization of the viscoelastic behavior of bituminous materials (Kim and Buttlar, 2009; You,2003) and is used herein for binder behavior at the low temperatures. In DEM, Burger's model has two dimensions and its properties are defined in normal/shear directions together before simulations are commenced, as shown in Fig. 3. Viscoelastic behavior is active in both directions and needs 9 parameters as follows- *Kkn* is the normal stiffness for the Kelvin section; *Ckn* is the normal viscosity for the Kelvin section; *Kmn* is the normal stiffness for the Maxwell section; *Cmn* is the normal viscosity for the Maxwell section; *Kks* is the shear stiffness for the Kelvin section; *Cks* is the shear viscosity for the Kelvin section; *Kms* is the shear stiffness for the Maxwell section; *Cms* is the shear viscosity for the Maxwell section; and *Fric* is the friction coefficient (Itasca Consulting Group,2008).

CZMs have widely been used to simulate crack growth both in FEM and DEM. In DEM, CZMs are assigned to discrete elements and make it possible to characterize the post-peak behavior, which is observed in reality. One of the typical CZMs used in DEM has the bilinear form shown in Fig. 4 and its strength is defined in Equation (2). As shown, *Up*

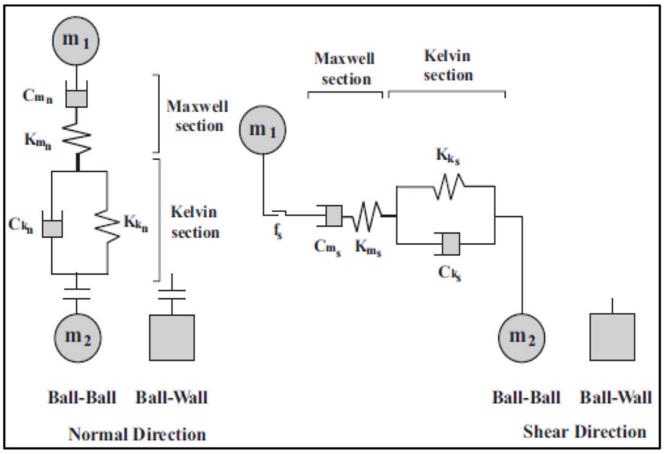

Fig. 3. Burger's model in DEM.

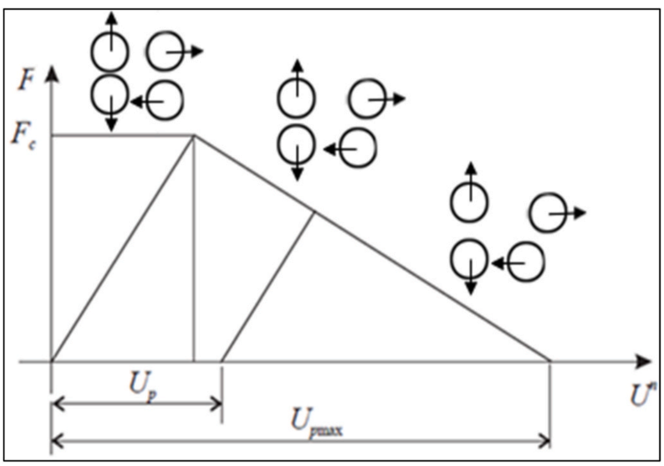

Fig. 4. CZM model in DEM.

represents the currently accumulated plastic displacement. When the contact exceeds the strength (*Fmax)*, the curves declines gradually and finally has no contact force when the maximum plastic displacement (*Upmax*) is reached. Bonding model can also solve balls' separations, but it cannot have a post-peak curve compared to CZM. Thus CZM model has priority in fracture simulations. The strength in Equation (2) is used to characterize the break of two adjacent elements in DEM rather than a given particle assembly.

$$F_{max} = \left(1 - \frac{2a}{\pi}\right) \bullet F_c^n + \frac{2a}{\pi} \bullet F_c^s \tag{2}$$

where, *Fmax* is the contact strength; *a* is the angle between the directions of the contact force and the line segment connecting the centers of the spheres; *Fcn* and *Fcs* are two strength parameters as a function of the current orientation of the contact force.

In summary, 7 parameters are needed to define the bilinear CZM as follows- *Sof_knc* is normal stiffness in compression; *Sof_knt* is normal stiffness in tension; *Sof_kns* is shear stiffness; *Sof_ftmax* is tensile strength; *Sof_fsmax* is shear strength; *Sof_fric* is friction coefficient; and *Sof_uplim* is accumulated plastic displacement for which the bond strength softens to zero.

The behavior of particles in the DEM not only depends on constitutive models but also on the elements' packing arrangements and sizes (Ding et al., 2020). To be consistent in parameter calibration process and final simulations, all the elements were generated as face-centered parking arrangements and set with a same radius of 0.0005m, as shown in Fig. 5. Different constitutive models need to be assigned to different compositions due to heterogeneity of rubber modified binders. For improving simulation efficiency, the ligament was established as ROI, as shown in Fig. 5. CZM was assigned to elements in the ligament area, burger's model and bonding model were applied out of the ligament area, and slipping model was active over the whole virtual specimens. After constitutive model assignments, parameters were determined based on a trial-and-error approach. For burger's model, slipping model and bonding model, the whole deflection curves of BBR were compared to optimize input parameters in PFC. Then, the F-CMOD curves of binder CT test were compared further between the reality and simulations to determine the parameters of CZM model.

3. Results and discussions

3.1. Verification of constitutive models

Trial-and-error approach was used for parameters determination. Firstly, four specimens were developed in DEM for BBR testing, including 0%, 8%, 10%, 12% GTR-modified binder (by weight). Then, parameters of Burger's model, bonding model and slipping model were calibrated as follows: the experimental and simulation test of unmodified binder were conducted to obtain the viscoelastic parameters for the base asphalt binder (binder-binder contact), and based on the results, randomly-placed rubber particles were generated as shown in Fig. 6(b) and (c). These random rubber particles were realized by coding logic in software with the help of 'Fish language'. It has a function of searching elements randomly and then set them as rubber particles. Using a trial-and-error approach, final model input parameters for rubber-binder contact was also determined and was summarized in Tables 2 and 3.

Fig. 7 presents verification of the Burger's model used in the BBR tests. As shown in Fig. 7, based on the experimental data, the rubber plays a positive role in softening the stiff binder at the low temperature (-12 °C). With more rubber added, the final deflection increases. The inversely-obtained bulk viscoelastic parameters were then applied to the binder CT test simulation.

As a nondestructive test, parameters of the bonding model were set as a relative high value in BBR simulations. For binder CT test, parameters in Tables 2 and 3 were assigned to contacts out of the ligament area and a hypothesis was made that cracks mostly appeared in the ligament area while cracks outside this area can be ignored. Thus, for the binder CT tests parameters of the bonding model were also set as a relative high value out of the ligament area. In the end, 10% GTR-modified binder were fractured in DEM and used to determine the final input parameters for CZM models in the ligament area, as shown in Table 3. Limited by the computer capacity, the BBR simulations were developed in 3 dimensions for parameters calibration. For the final binder CT developments, only 2 dimensions simulations were conducted due to its large specimen size. In 2D simulations, the general command named 'set disk off' in PFC were invoked. With the help of this command, the 2D disk in PFC2D is set as a 3D balls (the mass of 2D disk equals to the value of density multiplied by 3D-volume, rather than density multiplied by 2D-area, and thus affects the following movement equations). So the virtual binder CT model can be regarded as a two-dimensional slice of realistic 3D models. Thus, the dimension conversions can be converted more easily.

Input parameters in Tables 2–4 are average values when determined by trial-and-error approach in DEM simulations. These values were actually assigned to corresponding constitutive models at a Gaussian distribution, as shown in Equation (3).

$$Y = \frac{1}{\sqrt{2\pi} \bullet p} \bullet e^{\frac{-\left(urand^2 - 1 - u\right)^2}{2p^2}} + 0.5 \tag{3}$$

where Y is probability; *urand* is random value in DEM; *p,u* are shape parameters which are 0.4,0 respectively.

Thus, heterogeneous modeling was achieved in two ways when

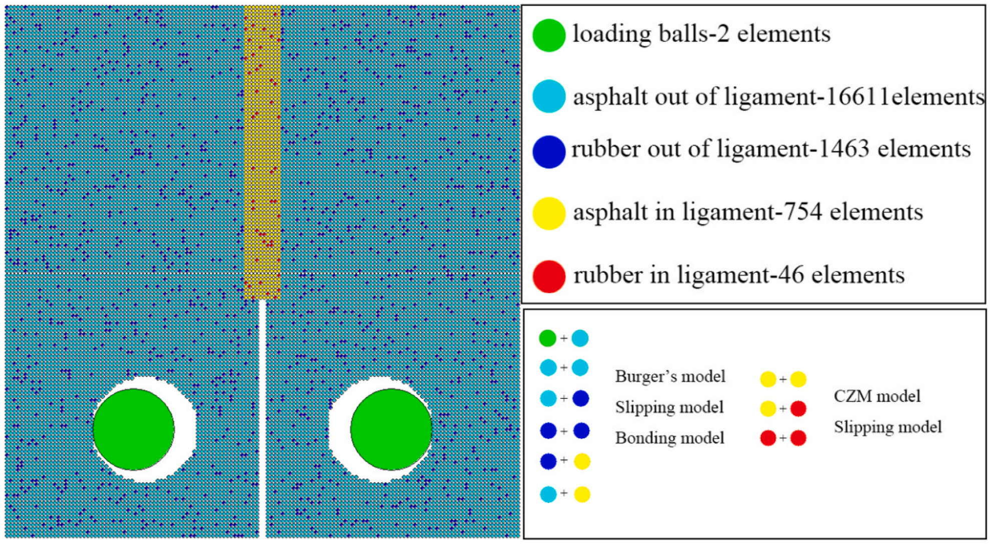

Fig. 5. Constitutive Model assignments in DEM.

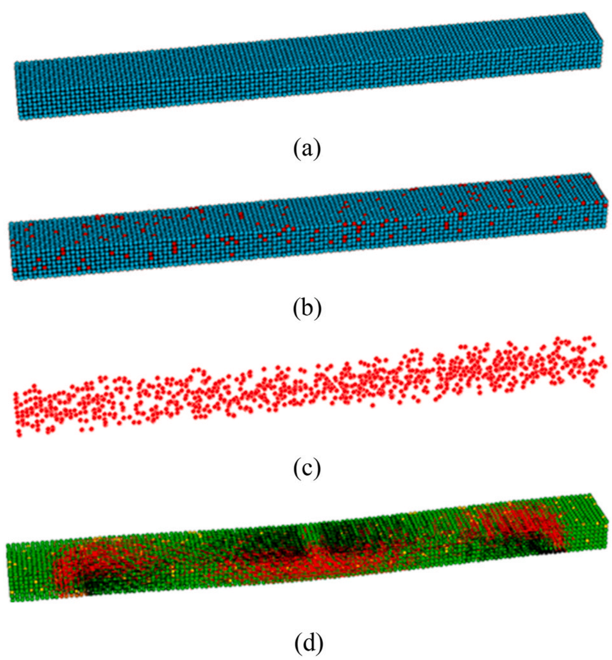

Fig. 6. BBR simulation: (a) unmodified binder; (b) rubber-modified binder; (c) random generation of rubber particles (10% content); (d) contact force distribution in BBR simulations (red line is tension force while black line is compression force).

modeled rubber modified binder testing, including random rubber particles generations as shown in Fig. 6(c), parameter assignments under Gaussian distribution as shown in Equation (3). Fig. 8 shows final results of binder CT test (10% GTR-modified binder). As shown, the simulation curve has a good fitting precision when compared to experimental one which verified the effectiveness of used constitutive models and their calibrated parameters.

3.2. Effects of rubber on binder

Four binder CT specimens were fractured in DEM as shown in Fig. 9, including 0%, 8%, 10%, 12% GTR-modified binder (by weight) and the effects of rubber particles on fracture resistance were illustrated from a global and a local perspective as shown in Figs. 10 and 11, respectively.

Fig. 10(a)–(b) shows the Load-CMOD curves and fracture energy values, respectively, for different rubber contents. The fracture energy was calculated based on the Specification, known as ASTM D7313 (American Society for Testing and Materials International,2013a). As shown in Fig. 10(a), unmodified binder behaves in a brittle fashion at the low temperature (-22 °C) and is fractured totally at CMOD of 0.36 mm. Conversely, GTR modified binder showed a ductile failure and rubber content influenced the global response significantly. With an increase in rubber content, the peak load increases and load can now be carried in the post-peak region, as shown in Fig. 10(a). The fracture energy for unmodified binder is 11.8 J/m^2 which is far less than GTR modified binders. The fracture energy of 12% GTR modified binder is almost 20 times of unmodified ones which shows that rubber modification plays a positive role in improving cracking resistance of binder at the low temperature.

Local response effects of rubber, which are not readily visualized in real experimental tests, were illustrated in DEM as shown in Fig. 11. Fig. 11(a) shows the force distributions when crack initiates and propagates. The pink and green elements are rubber particles in ligament and out of ligament respectively. As shown, granular rubber particles impede crack development to a point where the crack has fractured through the binder in the vicinity of the particles but is unable to navigate through the rubber particle. This forces the crack to circumvent

Table 3
Parameters of Bonding model and slipping model in DEM.

type	*nbond*	*sbond*	*fric*
asphalt+asphalt	5.2	3.8	0.5
asphalt+rubber	7.5	5.5	

Table 2
Parameters of Burger's model in DEM.

type	*Kkn*	*Ckn*	*Kmn*	*Cmn*	*Kks*	*Cks*	*Kms*	*Cms*	*Fric*
asphalt+asphalt	8e4	3.7e5	4e6	1.5e7	8e4	3.7e5	4e6	1.5e7	0.5
asphalt+rubber	5e4	3e5	9e5	8e6	5e4	3e5	9e5	8e6	0.5

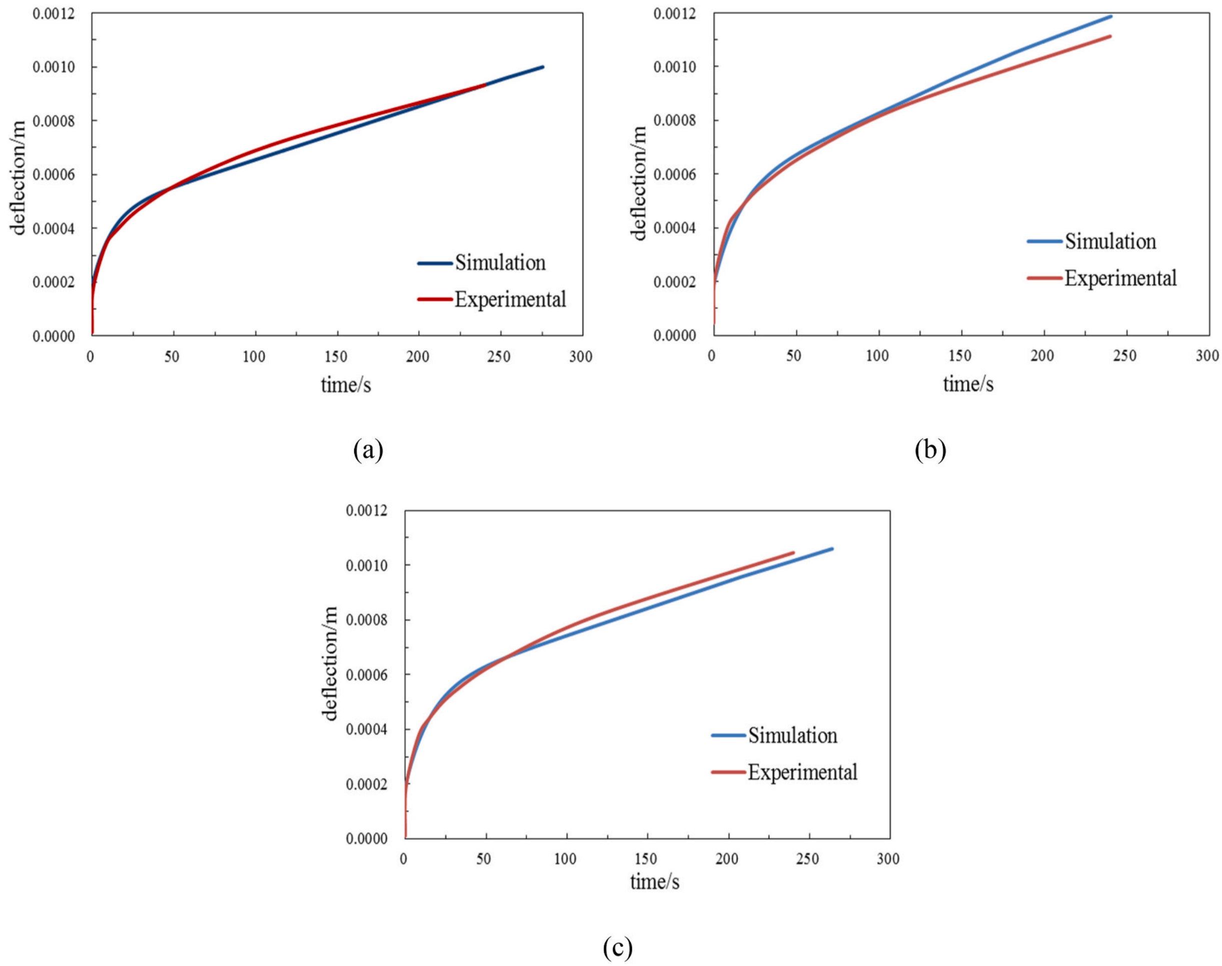

Fig. 7. Verification of viscoelastic parameters: (a) 8%GTR, (b) 10%GTR, (c) 12%GTR.

Table 4
Parameters of CZM model in DEM.

type	*Sof_knc*	*Sof_knt*	*Sof_kns*	*Sof_ftmax*	*Sof_fsmax*	*Sof_fric*	*Sof_uplim*
asphalt+asphalt	1e6	8e5	2e5	1.5	1	0.5	8e-4
asphalt+rubber	3e5	1e5	1e5	6	3	0.5	9e-4

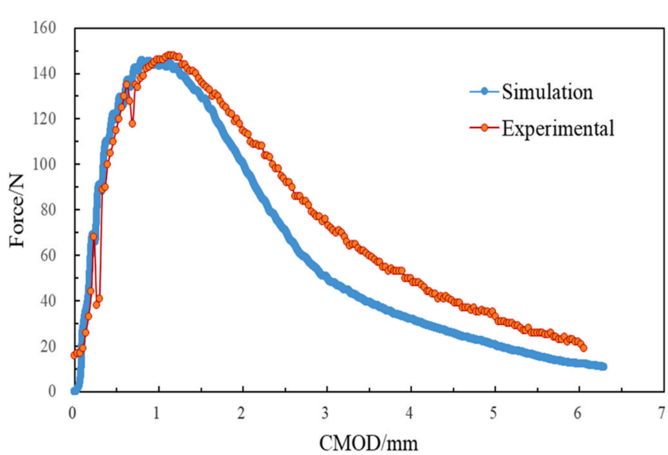

Fig. 8. Verification of viscoelastic and fracture parameters.

the particle (longer and tortuous paths to form new surfaces), resulting in a higher fracture energy. Fig. 11(b) is another version of Fig. 11(a) which shows the distributions of micro-cracks in simulations. The blue elements in Fig. 11(b) are rubber particles and black lines are marks outputted in DEM which means the disbanding of adjacent elements. When elements separated from each other, constitutive models applied here previously will not be active anymore. The positions of these marks are the same as current inactive contacts and their length equal to diameters of adjacent elements. It has been well-known that visible macro-cracks in most materials are formed due to coalescence of invisible micro-cracks. Previous findings by the authors (Ding et al., 2019) captured micro-cracks based on high-precision devices but could not make the crack evolutions clear enough.

As shown in Fig. 11(b), before crack tip grew, micro-cracks are more easily formed around rubber particles and need more energy for fracturing. This will delay the coalescence of these micro-cracks leading to a slow propagation of crack. The reason for this phenomenon is attributed to the uneven stiffness distributions in modified binders. In reality, rubber particles are dissolved partly and swelled in neat binder. It

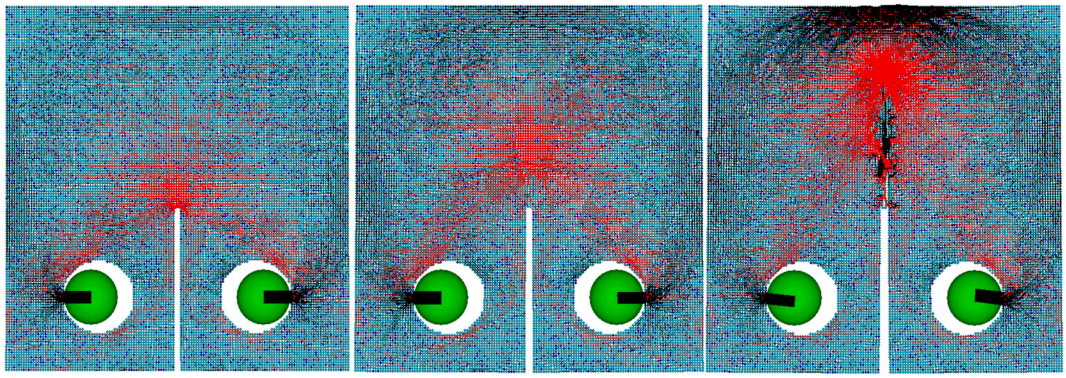

Fig. 9. Fracture modeling of binder CT tests.

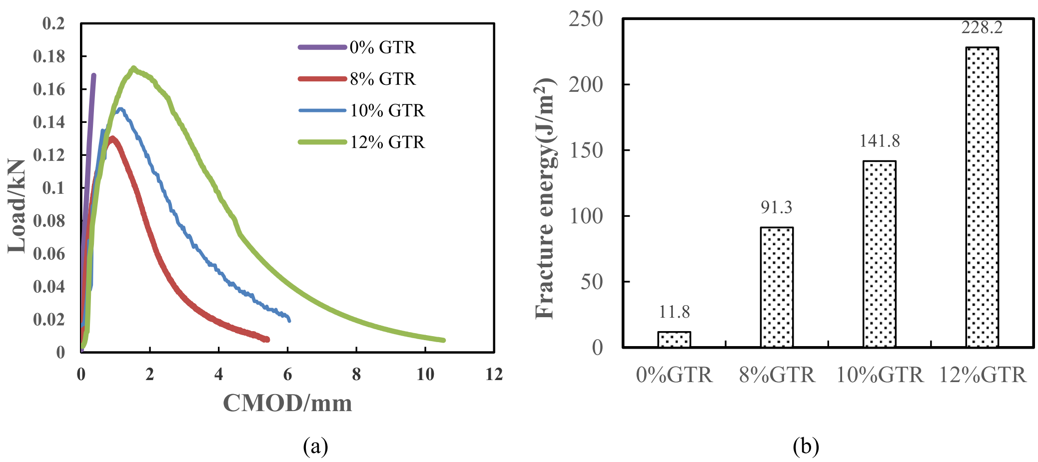

Fig. 10. Simulation results of binder CT test: (a) Load-CMOD curve, (b) Fracture energy.

softened neat binder at the low temperature and formed a transition region around itself (Rath et al., 2022). Compared to the neat binder, this transition region has a lower stiffness due to the softened rubber particles. So compared to the neat binder, when subjected to a same micro-strain, stiff neat binder will have larger stresses compared to rubber-modified binder. At the same time, rubber particles show a better bonding effect which has a higher strength than neat binder, as shown in Fig. 11(a). So in summary, transition region due to these dissolved rubbers has a lower stiffness but higher strength than neat binder and thus micro-cracks are more easily formed around rubber particles when subjected to same external loads.

3.3. Virtual FPZ evolution

Fracture Process Zone (FPZ) mainly grows ahead of the crack tip and this area tends to have plastic deformation leading to groups of micro-cracks [10]. The force distribution was set as a criterion in DEM and then the FPZ was defined based on it, as shown in Fig. 12. Contact force of all the elements were recorded and outputted at different CMOD. Most of them remained at a relative low value while part of them had a high value which should be regarded as elements from the FPZ. A standard criterion was set for FPZ recognitions during different periods. Linear regression was developed for contact force curves. The intercept on the vertical axis means critical point which differentiates FPZ and others. Abrupt change in contact state is another property of FPZ (similar to displacement changes). Thus, any elements subjected to a contact force larger than this critical point are defined as FPZ. And then FPZ size can be got by single element area multiplied by FPZ elements number (yellow ones in Fig. 12).

0%, 8%, 10%, 12% GTR-modified binder were fractured in DEM simulations and the crack length, crack number, FPZ size and average contact force in FPZ for each of them were monitored and recorded as shown in Figs. 13–15. For brevity, only simulation images of 10% GTR modified binders are presented hereafter in Fig. 13.

In Fig. 13, yellow lines are FPZ elements while blue lines are accumulated micro-crack marks. Based on the principle of DEM coding, FPZ can be displayed in real-time since they are defined based on the real-time contact force distributions. So FPZ in Fig. 13 increases initially to reach peak value and then decreases gradually. However, micro-cracks are accumulated ones in PFC because these disbanding marks will be displayed in software all the time when the contact breaks and will not disappear in the following calculation steps. Thus, this display fashion can show path and evolution details of fracture prorogation in binder CT simulations. As shown, FPZ has a narrow and long shape along loading directions in front of crack tip. Micro-cracks form and coalesce to a visible macro crack as the CMOD increase which is consistent with observations from experiments. But interesting findings show that micro-cracks initiate at CMOD of 0.22 mm in pre-peak area rather than at peak-load for 10% GTR modified binders. And the maximum value of FPZ size is located in the post-peak area rather than at peak-load as well. These new findings can be seen from simulation images in Fig. 13 and similar results of different rubber content are also summarized in Figs. 14 and 15. The whole process of micro-crack propagation and FPZ evolution was revealed at different CMOD period as shown in Fig. 13. This work will help understand the micro-mechanism of rubber particles interacting with binder and thus can optimize materials design from the point of improving anti-cracking property. Moreover, the method of revealing micro-crack behavior herein is also an effective way for

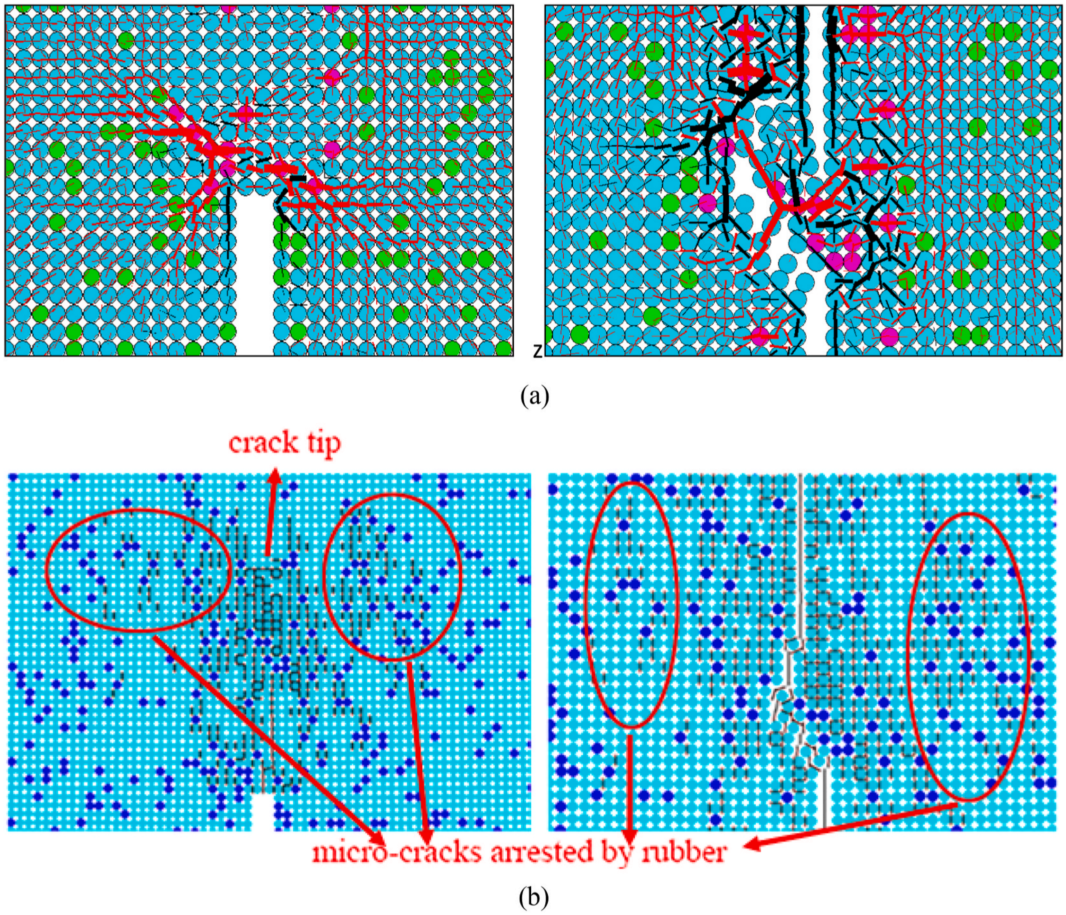

Fig. 11. Micro analysis of crack propagation in binder: (a) force distribution; (b) coalescence of micro-cracks.

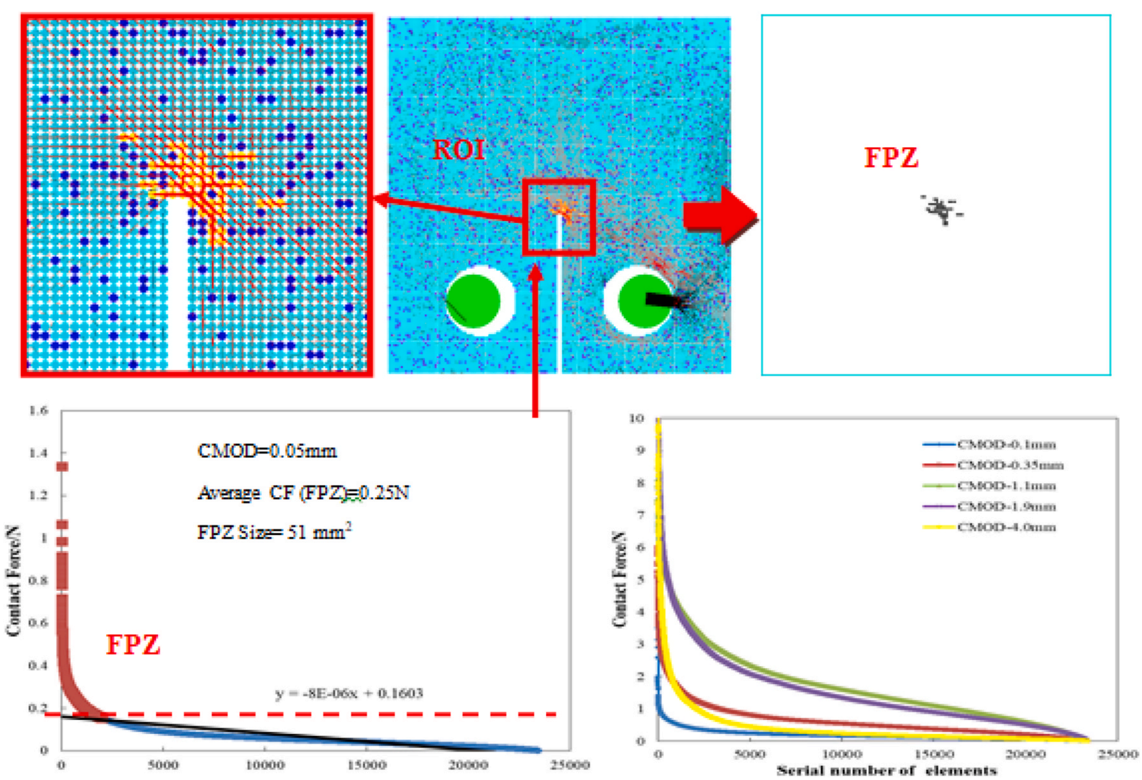

Fig. 12. Virtual FPZ recognition and development.

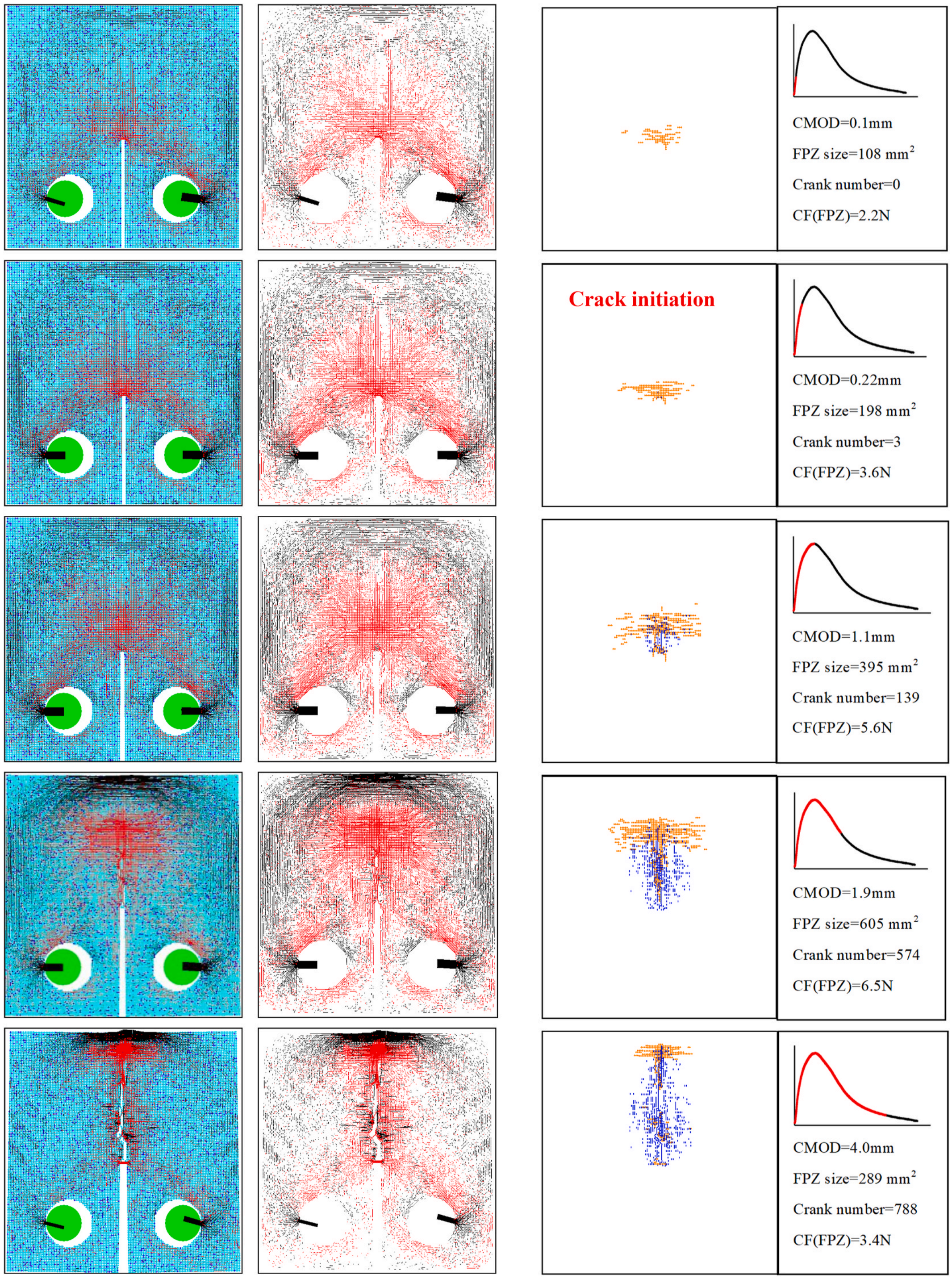

Fig. 13. Evolutions of micro cracks and FPZ in binder CT test at different CMOD.

pavement performance assessment in future. Based on the micro-crack analysis, the damage degree at any time can be known which helps early warning precisely in pavement healthy monitoring.

As shown in Fig. 10(a), unmodified binder shows a brittle failure and fractured totally at CMOD of 0.36 mm with load of 0.168 kN, while rubber modified binder shows ductile failure and has a post-peak area. The peak loads of 8%, 10%, 12% modified binders are 0.129 kN at CMOD of 0.73 mm, 0.151 kN at CMOD of 1.1 mm and 0.172 kN at CMOD of 1.7 mm, respectively. Fig. 14 demonstrates crack evolutions of unmodified and modified binder in designed fracture tests, including crack length and crack number. As shown in Fig. 14(a), as CMOD increases, the crack length has a linear growth at most of the test time and the slopes for rubber modified binders tend to decrease when crack tip moves near upper boundary.

Compared to rubber modified binders, unmodified curve has the largest slope meaning that macro-crack propagates at a really fast speed in brittle fashion and cannot be subjected to a large displacement. The additions of rubber can slow down the propagation speed of macro-cracks which explains reasons for higher fracture energy of GTR modified binders. Fig. 14(b) illustrates micro-crack evolutions during different CMOD periods. The crack number of unmodified binders increased sharply at the beginning and broke rapidly at a low CMOD.

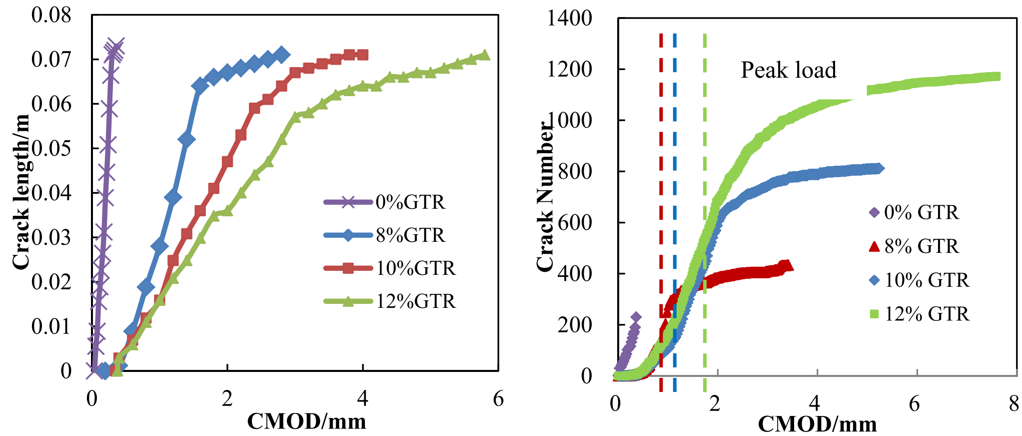

(a) (b)

Fig. 14. Summaries of crack evolutions in binder CT test: (a) crack length; (b) crack number.

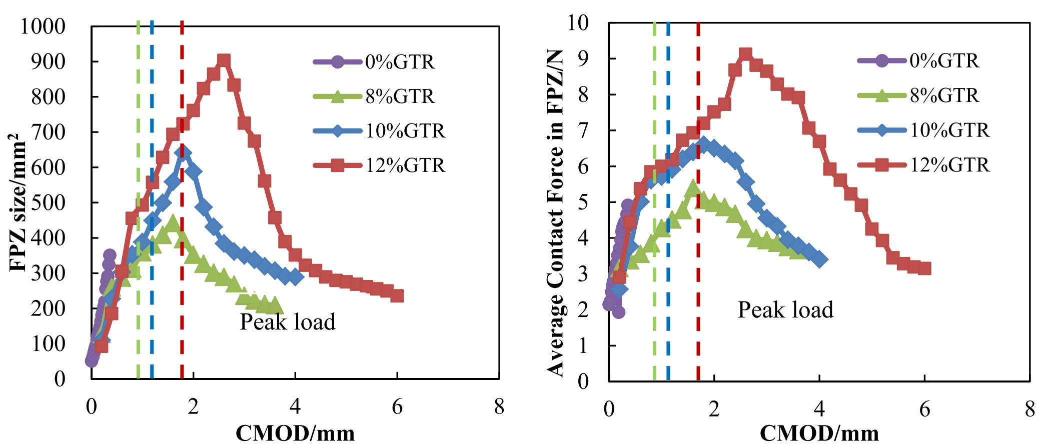

(a) (b)

Fig. 15. Summaries of FPZ evolutions in binder CT test: (a) FPZ size; (b) average contact force in FPZ.

Although the slopes of crack number curves are lower for rubber modified binders at beginning, they have a larger CMOD area and thus generate more micro-cracks during the whole periods, especially in post-peak area which accounts for 50–60% of total crack numbers. And the rubber content plays a positive role in increasing the number of micro-cracks when fractured as shown in Fig. 14(b). The total number of micro-cracks in 12% GTR modified binder is nearly 3 times of that in 8%GTR modified binder, and 6 times of that in unmodified binder. The micro-crack initiates at CMOD of 0.032 mm, 0.196 mm, 0.220 mm and 0.286 mm for unmodified, 8%, 10%, 12% modified binders respectively. It is also observed that the rubber delays micro-crack initiations in front of crack tip during the initial phase of fracture testing.

Fig. 15 are summaries of FPZ evolutions in binder CT tests for different binders, including FPZ size and average contact force in FPZ. As shown, these evolutions curves are similar to Load-CMOD curve which also has a pre-peak, post-peak trend for modified binders and a linear growth for unmodified binder without any post-peak behaviors. With more rubber added in the binder, the specimens will have larger FPZ and the average contact force in FPZ increases. This is because the dissolved rubber particles soften binder and decrease the stiffness of the total heterogeneous materials and thus generate larger FPZ. Interesting findings are also shown that similar to the results of crack initiations, the maximum value of FPZ locates at the post-peak area for all the modified binders, mainly located within 0.7–0.9 mm after peak load depending on rubber contents.

Figs. 16 and 17 show the results of dissipated energy monitored in binder CT simulations. In reality, any destructive experimental tests are inclusive of the materials' nondestructive behaviors, which are represented by the FPZ. During experiments, energy is inputted by the loading system and consumed by heterogeneous binder. Part of energy is consumed for generating new surfaces and then forms micro-cracks. The rest of energy is stored in materials with the form of nondestructive deformation, such as plastic deformation in FPZ etc. From the perspective of numerical calculations, the transfer of energy in simulations depends on the mathematical model and results from the simulations carried in this study are shown in Figs. 16 and 17.

In Fig. 16, the blue bar means the energy consumed for real micro-cracks in simulations. When parameters of CZMs has been determined, the shape of CZM is known and energy consumed for single particles' break can be calculated. Based on the micro-cracks evolutions, total energy consumed for real cracks can be determined. The red bar in Fig. 16 means other dissipated energy in fracture simulations due to the combined use of different constitutive models including: (1) dissipated energy for friction; (2) kinetic energy; (3) energy caused by CZM models

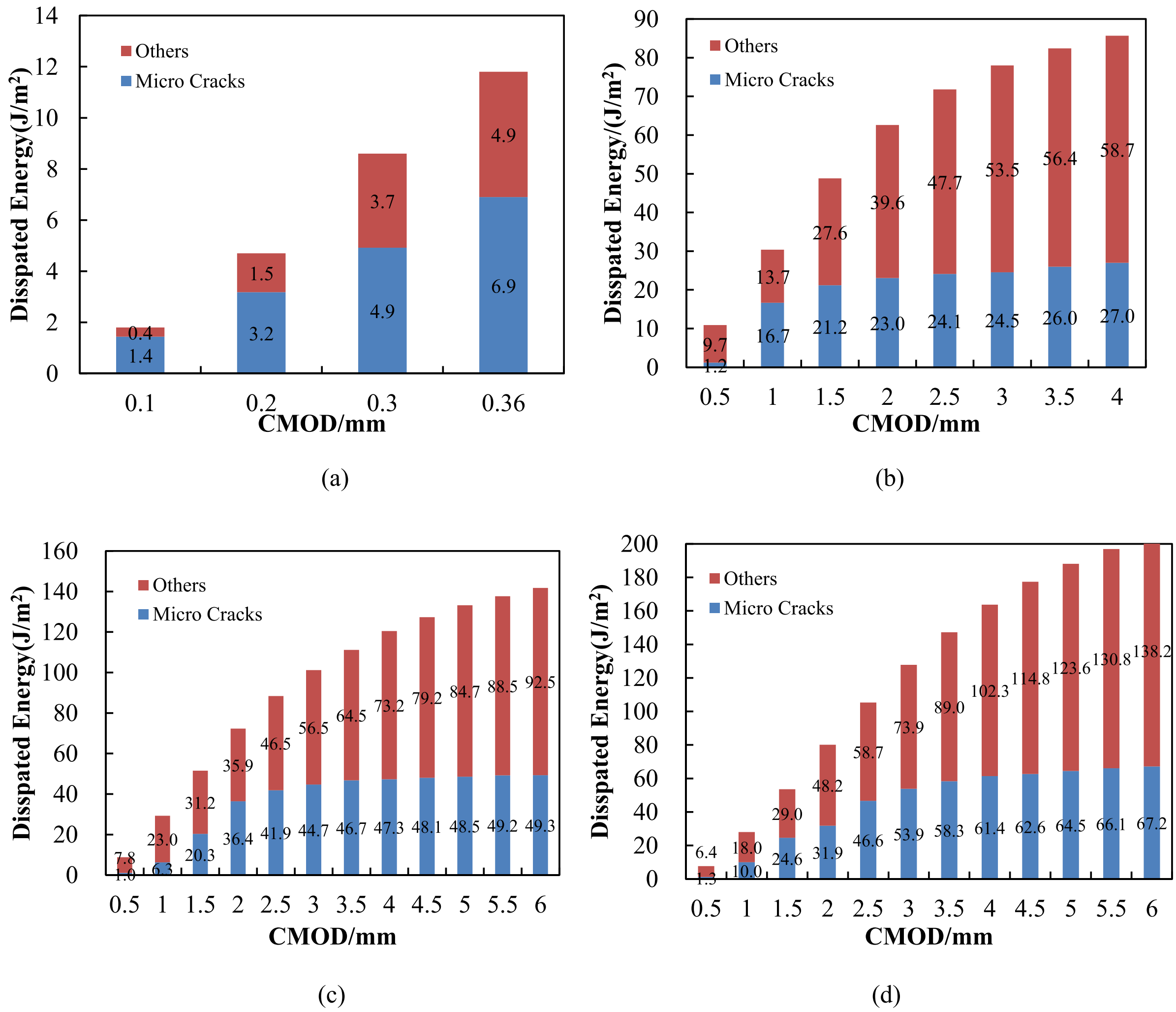

Fig. 16. Summaries of dissipated energy in binder CT test: (a) 0%GTR; (b) 8%GT; (c) 10%GTR; (c) 12%GTR.

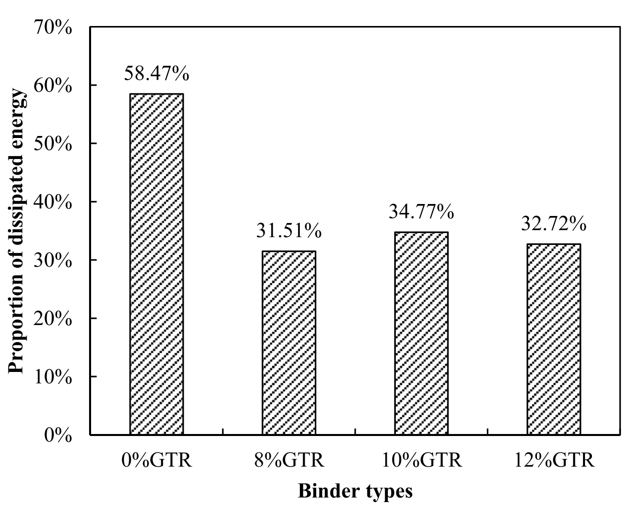

Fig. 17. Proportion of dissipated energy for real cracks to measured one (compared when specimen fractured totally).

which doesn't break and is stored as elastic energy; (4) energy caused by burger's models (energy stored in spring and dissipated due to dashpot). The sum of red and blue bars is fracture energy measured based on Load-CMOD curves in simulations [10]. As shown in Fig. 16, the other dissipated energy in simulations cannot be ignored and accounts for 50%–70% of different binders. It explains that the nondestructive deformations in macro experimental tests also play an important role and thus it may not be suitable when use measured fracture energy [33] to represent the fracture resistance of tested binders in further smaller scale. Fracture energy measured is suitable for macro experimental evaluations but dissipated energy for real micro cracks should be set as assessment criteria when conducting numerical analysis at a smaller scale.

As shown in Fig. 16, dissipated energy of rubber modified binders are much larger than unmodified one. As the rubber contents increase, more energy is consumed by real micro-cracks and nondestructive deformations. The trends of blue bar in Fig. 16 are similar to that in Fig. 14 because this energy is calculated based on crack numbers. On comparing Figs. 14 and 16, it can be shown that micro-cracks increase slowly towards the end of the post-peak area and nondestructive deformations dominate during this period of time. Fig. 17 illustrates the proportions of dissipated energy for real cracks to measured fracture energy when virtual specimens fractured totally. It is concluded that with more rubber added in neat binder, the specimens will have a higher ability to be subjected to nondestructive deformations and that's why FPZ increases in rubber modified binders. Increased dissipated energy for this nondestructive deformation also leads to improvement of measured fracture energy. Moreover, the energy consumed by the real cracks in simulations also increase at the same time when the rubber content increase. Thus, it proves the positive effect of rubber particles on improving anti-cracking resistance at the low temperature from a smaller research scale based on authors' simulation analysis.

4. Conclusions

This study developed numerical models for a modified binder fracture test, referred to as the binder CT test, and analyzed the fracture mechanism at the micro scale. Several important indices were evaluated including fracture energy under Load-CMOD curves, dissipated energy for micro-cracks, morphology of micro-cracks and FPZ. The following conclusions can be drawn from the results of this investigation:

(1) The combined use of Burger's model and CZM model has been verified which can characterize the viscoelastic and fracture behaviors well of unmodified and rubber modified binders. It is an effective way to develop heterogeneous modeling by random rubber particles generations and parameter assignments under Gaussian distribution.
(2) The unmodified binder behaves a brittle failure at the low temperatures while rubber modified binders have a ductile failure mode. With the increase of rubber content, the modified binder tends to have a larger peak load, better post-peak curve and larger fracture energy which proves the positive role the rubber particles play in improving the fracture resistance at the low temperature from the perspective of macro-behavior analysis.
(3) Based on micro simulations, it is found that micro-cracks initiate in the pre-peak region rather than at the peak-load. The micro-cracks mainly initiates at CMOD values between 0.2 mm and 0.3 mm, depending on different rubber contents. The rubber slows down the process of micro-crack initiations when fracture testing starts. The micro-cracks develop rapidly in the pre-peak area and in the front part of post-peak area and then the growth rate decreases in the rear part of post-peak area. During this period of time, the nondestructive deformation dominates and consumes most of the energy. Compared to the rubber modified binder, unmodified one has fewer micro-cracks and less nondestructive deformation during the whole process which leads to an abrupt decline in fracture energy.
(4) The dissolved rubber particles will form a transition region around themselves with lower stiffness but higher strength as compared to those of the neat binder. When crack tip propagates, it provides a better bonding effect and impedes crack development to a point where the crack has fractured through the binder in vicinity of the particles but is unable to navigate through the rubber particle. This forces the crack to circumvent the particle and has longer and tortuous paths to form new surfaces. At the same time, due to the differences of stiffness and strength in transition region, micro-cracks tend to develop in some weak area around rubbers. It delays the coalescence of these micro-cracks leading to a slow speed of macro crack length and thus need more energy consumed. In summaries, both reasons result in higher fracture energy for rubber modified binders.
(5) The rubber plays a positive role in FPZ size and average contact force in FPZ. The evolutions of FPZ size and average contact force in it have a similar shape to Load-CMOD curves which also have a pre-peak, post peak area for rubber modified binders while there are no post-peak curves for unmodified binders. The maximum value of FPZ locates at the post-peak area for all the modified binders, mainly locates within 0.7–0.9 mm after peak load depending on rubber contents which cannot be got from experimental tests. With the increase of rubber content, FPZ size and contact force in it increases as well which means a corresponding growth of nondestructive deformations in reality. And it needs more energy to be stored in FPZ and is verified in simulations. That's another reason for higher fracture energy of rubber modified binders.
(6) Dissipated energy for real micro-cracks were divided from the whole. It is concluded that energy consumed for nondestructive deformations cannot be ignored since they accounts for almost 50%–70% of all during the whole process. It may not be suitable when use measured fracture energy to represent the anti-crack resistance of tested binders completely in further smaller scale. But similar results are found that rubber modified binder has a higher dissipated energy for real micro-cracks than unmodified one. And the differences of dissipated energy become more obvious as the rubber content increases.

CRediT authorship contribution statement

Xunhao Ding: Fracture simulation, analysis and draft manuscript preparation. **Punyaslok Rath:** Fracture test design and testing data collection. **Oliver Giraldo-Londoño:** Manuscript revision. **William G. Buttlar:** Project leader and supervisor. **Tao Ma:** Project leader and supervisor.

Declaration of competing interest

The authors declare that they have no known competing financial interests or personal relationships that could have appeared to influence the work reported in this paper.

Data availability

The data that has been used is confidential.

Acknowledgments

The study is financially supported by the National Natural Science of Foundation of China(NO.52208427), Natural Science Foundation of Jiangsu(BK20220844), Graduate Innovation Project of Jiangsu Province (KYCX18_0147), Scientific Research Foundation of the Graduate School of Southeast University (YBJJ1843) and the Chinese Scholarship Council (No.201906090216).

References

Abbas, A., Masad, E., Papagiannakis, T., Harman, T., 2007. Micromechanical modeling of the viscoelastic behavior of asphalt mixtures using the discrete-element method. Int. J. GeoMech. 7 (2), 131–139.
American Society for Testing, Materials International, 2000. Standard Test Method for Viscosity Determination of Asphalt at Elevated Temperatures Using a Rotational Viscometer. ASTM D4402, West Conshohocken, PA.
American Society for Testing, Materials International, 2013a. Standard Test Method for Determining Fracture Energy of Asphalt-Aggregate Mixtures Using the Disk-Shaped Compact Tension Geometry. ASTM, West Conshohocken, PA. D7313.
American Society for Testing and Materials International, 2013b. Standard Test Method for Linear-Elastic Plane-Strain Fracture Toughness KIc of Metallic Materials. ASTM, West Conshohocken, PA. E399.
American Society for Testing, Materials International, 2016. Standard Test Method for Determining the Flexural Creep Stiffness of Asphalt Binder Using the Bending Beam Rheometer (BBR). ASTM, West Conshohocken, PA. D6648.
Behnia, B., Dave, E.V., Buttlar, W.G., Reis, H., 2016. Characterization of embrittlement temperature of asphalt materials through implementation of acoustic emission technique. Construct. Build. Mater. 111, 147–152.
Braz, D., Barroso, R.C., Lopes, R.T., Motta, L.G., 2011. Crack detection in asphaltic mixtures by computed tomography. NDT E Int. 44 (2), 195–201.
Buttlar, W.G., Hill, B.C., Kim, Y.R., Kutay, M.E., Millien, A., Montepara, A., et al., 2014. Digital image correlation techniques to investigate strain fields and cracking phenomena in asphalt materials. Mater. Struct. 47 (8), 1373–1390.
Cundall, P.A., Strack, O.D.L., 1980. Discussion: a discrete numerical model for granular assemblies. Geotechnique 30 (3), 331–336.
Dave, E.V., Behnia, B., Ahmed, S., Buttlar, W.G., Reis, H., 2011. Low temperature fracture evaluation of asphalt mixtures using mechanical testing and acoustic emissions techniques. Asphalt Paving Technology: Association of Asphalt Paving Technologists-Proceedings of the Technical Sessions 80, 193–220.

Ding, X., Ma, T., Gu, L., Zhang, Y., 2019. Investigation of surface micro-crack growth behavior of asphalt mortar based on the designed innovative mesoscopic test. Mater. Des. 185, 108238.

Ding, X., Ma, T., Gu, L., Zhang, D., Huang, X., 2020. Discrete element methods for characterizing the elastic behavior of the granular particles. J. Test. Eval. 48 (3).

Fan, C., Jar, P.Y.B., Cheng, J.J.R., 2007. Prediction of energy release rates for crack growth using FEM-based energy derivative technique. Eng. Fract. Mech. 74 (8), 1243–1254.

Gajewski, J., Sadowski, T., 2014. Sensitivity analysis of crack propagation in pavement bituminous layered structures using a hybrid system integrating artificial neural networks and finite element method. Comput.Int. J. Pavement Res. Technol. Mater. ence 82, 114–117.

Gilbert, Strang, 1974. An analysis of the finite element method. Math. Comput. 41 (1), 115–126.

González, V., Martínez-Boza, F.J., Navarro, F.J., et al., 2010. Thermomechanical properties of bitumen modified with crumb tire rubber and polymeric additives. Fuel Process. Technol. 91 (9), 1033–1039.

Hakimzadeh, S., Behnia, B., Buttlar, W.G., Reis, H., 2017. Implementation of nondestructive testing and mechanical performance approaches to assess low temperature fracture properties of asphalt binders. Int. J. Pavement Res. Technol. 10 (3), 219–227.

Hill, B.C., Giraldo-London, O., Paulino, G.H., Buttlar, W.G., 2017. Inverse estimation of cohesive fracture properties of asphalt mixtures using an optimization approach. Exp. Mech. 57 (4), 637–648.

Imaninasab, R., Bakhshi, B., Shirini, B., 2016. Rutting performance of rubberized porous asphalt using finite element method. Construct. Build. Mater. 106, 382–391.

Itasca Consulting Group, 2008. PFC2D Manual Ver. 4.0. Minneapolis.

Kim, H., Wagoner, M.P., Buttlar, W.G., 2008. Simulation of fracture behavior in asphalt concrete using a heteroge-neous cohesive zone discrete element model. J. Mater. Civ. Eng. 20 (8), 552–563.

Kim, H., Buttlar, W.G., 2009. Discrete fracture modeling of asphalt concrete. Int. J. Solid Struct. 46 (13), 2593–2604.

Lancaster, I.M., Khalid, H.A., Kougioumtzoglou, I.A., 2013. Extended FEM modelling of crack propagation using the semi-circular bending test. Construct. Build. Mater. 48 (nov), 270–277.

Lee, S.J., Kim, H., Akisetty, C.K., Amirkhanian, S.N., 2008. Laboratory characterization of recycled crumb-rubber-modified asphalt mixture after extended aging. Can. J. Civ. Eng. 35 (11), 1308–1317.

Mull, M.A., Stuart, K., Yehia, A.A., 2002. Fracture resistance characterization of chemically modified crumb rubber asphalt pavement. J. Mater. Sci. 37 (3), 557–566.

Rath, P., Love, J.E., Buttlar, W.G., Reis, H., 2019a. Performance analysis of asphalt mixtures modified with ground tire rubber modifiers and recycled materi-als. Sustainability 11 (6), 1792.

Rath, P., Majidifard, H., Jahangiri, B., Buttlar, W.G., 2019b. Recent advances in ground tire rubber recycling in midwest pavements. In: Association of Asphalt Paving Technologists. AAPT, Fort Worth, Texas, pp. 1–29.

Rath, P., Gettu, N., Chen, S., Buttlar, W.G., 2022. Investigation of cracking mechanisms in rubber-modified asphalt through fracture testing of mastic specimens. Road Mater. Pavement Des. 23 (7), 1544–1563.

Sienkiewicz, M., Borzędowska-Labuda, K., Wojtkiewicz, A., Janik, H., 2017. Development of methods improving storage stability of bitumen modified with ground tire rubber: a review. Fuel Process. Technol. 159, 272–279.

Song, S.H., Paulino, G.H., Buttlar, W.G., 2015. Simulation of crack propagation in asphalt concrete using an intrinsic cohesive zone model. J. Eng. Mech. 132 (11), 1215–1223.

Themeli, A., Chailleux, E., Farcas, F., Chazallon, C., Migault, B., 2016. Modeling the linear viscoelastic behavior of asphaltite-modified bitumens. Rheol. Acta 55 (11–12), 1–13.

Wang, H., Dang, Z., Li, L., You, Z., 2013. Analysis on fatigue crack growth laws for crumb rubber modified asphalt mixture. Construct. Build. Mater. 47, 1342–1349.

Wang, H., Buttlar, W.G., 2019. Three-dimensional micromechanical pavement model development for the study of block cracking. Construct. Build. Mater. 206, 35–45.

You, Z., 2003. Development of a Micromechanical Modeling Approach to Predict Asphalt Mixture Stiffness Using the Discrete Element Method (Doctoral dissertation).

Yuan, J., Lv, S., Peng, X., You, L., Cabrera, M.B., 2020. Investigation of strength and fatigue life of rubber asphalt mixture. Materials 13 (15), 3325.

Yan, K., Wang, S., Ge, D., Chen, J., Sun, H., 2020. Laboratory performance of asphalt mixture with waste tyre rubber and apao modified asphalt binder. Int. J. Pavement Eng. (1), 1–11.

Zhang, D., Hou, S., Bian, J., He, L., 2016. Investigation of the micro-cracking behavior of asphalt mixtures in the indirect tensile test. Eng. Fract. Mech. 163, 416–425.